Simulations of the optical properties of warm dense aluminum

S. Mazevet,[1] M. P. Desjarlais,[2] L. A. Collins,[1] J. D. Kress,[1] and N. H. Magee[1]
[1]*Theoretical Division, Los Alamos National Laboratory, Los Alamos, New Mexico 87545, USA*
[2]*Pulsed Power Sciences Center, Sandia National Laboratories, Albuquerque, New Mexico 87185, USA*
(Received 15 June 2004; published 19 January 2005)

Using quantum molecular dynamics simulations, we show that the optical properties of aluminum change drastically along the nonmetal metal transition observed experimentally. As the density increases and the many-body effects become important, the optical response gradually evolves from the one characteristic of an atomic fluid to the one of a simple metal. We show that quantum molecular dynamics combined with the Kubo-Greenwood formulation naturally embodies the two limits and provides a powerful tool to calculate and benchmark the optical properties of various systems as they evolve into the warm dense matter regime.

DOI: 10.1103/PhysRevE.71.016409 PACS number(s): 52.25.Os, 52.65.Yy, 61.20.Ja, 62.50.+p

I. INTRODUCTION

Recent developments in a wide variety of fields, including dense plasmas [1], inertial confinement fusion [2], and astrophysics [3,4], require an improved understanding of the optical properties of various media into new and complex regimes. The relatively low-temperature, high-density regime (a few eV, a few g/cm^3), often labeled as "warm dense matter" (WDM), provides an example of such a situation where the intricate nature of the medium - partially dissociated, ionized, and degenerate makes the modelling of the dynamical, electrical, and optical properties extremely challenging. In this regime, reached experimentally by shock compression in the Mbar range [1,5–7], laser heating of solid targets [8–10], or exploding wires [11–14], many-body effects are such that the calculation of the optical properties using standard atomic physics models [15] quickly becomes unreliable [16].

Quantum molecular dynamics simulations (QMD) [17,18], where the active electrons receive a full quantum mechanical treatment within the finite temperature density functional theory (FT-DFT), offers an opportunity to improve this situation by providing a venue to calculate the optical properties of complex plasmas in this difficult regime. When combined with the Kubo–Greenwood formulation, the method produces a consistent set of material, electrical, and optical properties from the same simulation and can be applied without restriction to various mixtures of atomic, ionic, or molecular species. Over the past few years, QMD simulations have been used successfully to calculate the equation-of-state (EOS), electrical conductivity, and reflectivity of various systems such as hydrogen (H) [19–22], nitrogen (N) [23–25], aluminum (Al) [26], nitrogen oxide (NO) [27], and silica (SiO_2) [28].

In this paper, we extend our earlier application of the QMD method to the calculation of the optical properties of warm, dense hydrogen [19,20] to the more complex system aluminum and across the transition into the warm dense matter regime. Aluminum has been extensively studied in this regime, both experimentally and theoretically, and the variation of its conductivity for various density-temperature conditions has recently received considerable attention [8,11,13,14,26,29–31]. In contrast, the corresponding optical properties are far less known, essentially due to the difficulties in applying current opacity models at these particular conditions.

In the present paper, we particularly focus on densities and temperatures ranging from 0.025 g/cm^3 and 10 000 K to 2 g/cm^3 and 30 000 K. This region was extensively studied in a previous paper [26] where very good agreement was found between the calculated conductivities and data from exploding wire experiments [14]. The optical conductivities obtained there serve as the starting point for many of the optical properties calculated in this work. The experimental measurements and QMD simulations indicate a clear nonmetal to metal transition in this density-temperature region. At the lowest density, aluminum behaves as an atomic gas and evolves, as the density increases, into a strongly correlated plasma where correlation between the three valence electrons is important. We find that this nonmetal metal transition leads to drastic changes in the optical properties of the system consistent with the dramatic changes in the electrical properties. At the lowest density, the absorption coefficient and associated index of refraction show features characteristic of a system in a mostly atomic state. As the density increases and the media evolves into the warm dense matter regime, these features gradually disappear and evolve into the one characteristic of a simple metal. We show that QMD simulations naturally embody the two limits and as such provide a powerful tool to calculate and benchmark the optical properties of various systems in the difficult regime where standard opacity calculations based on isolated atom properties usually fail.

II. THEORETICAL METHOD

We briefly review the main points of our QMD approach. Specific details of the QMD simulations for aluminum used here may be found in Ref. [26]. Further details on the QMD method in general can be found in earlier publications [19–21,25].

A. Molecular dynamics simulations

The particular implementation of the QMD method used in the present work comes from the VASP (Vienna *Ab Initio*

Simulation Program) plane-wave code, developed at the Technical University of Vienna [32]. Within this code, a fixed-volume reference cell of N-atoms, periodically replicated throughout space, forms the basis of the simulation. After invoking the Born-Oppenheimer approximation, the active electrons, usually corresponding to the valence electrons of the atomic species considered, are treated fully quantum mechanically using a finite-temperature (T_e) density functional (FT-DF) calculation [33] in the generalized gradient approximation (GGA). This produces, for the N_e active electrons a set of n_b orbitals $\Psi_{i,\mathbf{k}}$ and energies $\epsilon_{i,\mathbf{k}}$ for a particular **k**-point in the Brillouin zone of the reference cell within the usual Kohn-Sham construction,

$$H_{\mathrm{KS}}\Psi_{i,\mathbf{k}} = \epsilon_{i,\mathbf{k}}\Psi_{i,\mathbf{k}}. \tag{1}$$

The program employs the Perdew-Wang 91 parametrization of the GGA [34] and provides two forms for the effective potential: the Vanderbilt ultrasoft (US) pseudopotential scheme [35] in a form supplied by Kresse and Hafner [36] and the projector augmented wave (PAW) method given by Kresse *et al.* [37,38].

We reiterate now for completeness the details of the QMD calculations in Ref. [26]. The US potential formulation, which requires a smaller plane-wave basis and therefore computational time, was usually employed for the long temporal QMD runs to produce a trajectory. The bulk of the QMD calculations were performed using only the Γ point for representation of the Brillouin zone (BZ) with a plane wave cutoff (E_{cut}) of 129 eV. Several (ρ, T) pairs were also examined with higher order **k**-point sets, such as the Monkhorst-Pack $2\times2\times2$ [39], or the Baldereschi mean value point [40], but with no significant effect on the various quantities of interest.

Each density temperature point was typically simulated for about 3 ps. To cover a broad range of densities, from 0.025 to 2.0 g/cm^3, the number of atoms used in the simulation cell was varied. For densities of 1.0 and 2.0 g/cm^3, the simulations were performed using 108 atoms. As the computational time increases with the number of plane waves, the number of atoms in the simulation cell was reduced for the lower densities to keep the computational time in bounds. For densities from 0.05 g/cm^3 up to 1.0 g/cm^3, the number of atoms was reduced to 32. For 0.05 and 0.1 g/cm^3, we performed simulations with 16 atoms, and dropped to as few as eight atoms in the simulation cell at the lowest density, 0.025 g/cm^3. At each reduction in the number of atoms in the simulation cell, comparisons were made between two simulation cells, at the same physical density, to rule out any significant size dependence in the calculation. In all cases these differences were within 10%.

B. Optical properties

Following the QMD simulations, a total of 10 to 20 configurations were selected from an equilibrated (in an average sense) portion of the molecular dynamics run, typically sampling the final picosecond of evolution. For each of these configurations, the optical conductivity was calculated using the Kubo-Greenwood formulation [41–43].

The Kubo-Greenwood formulation [41,43] gives the real part of the electrical conductivity, as a function of frequency ω, and at a particular **k**-point as

$$\sigma_1(\mathbf{k},\omega) = \frac{2\pi}{3\omega\Omega}\sum_{j=1}^{n_b}\sum_{i=1}^{n_b}\sum_{\alpha=1}^{3}[F(\epsilon_{i,\mathbf{k}}) - F(\epsilon_{j,\mathbf{k}})] \times \langle\Psi_{j,\mathbf{k}}|\nabla_\alpha|\Psi_{i,\mathbf{k}}\rangle^2\delta(\epsilon_{j,\mathbf{k}} - \epsilon_{i,\mathbf{k}} - \omega). \tag{2}$$

We employ atomic units, with the electron charge e, Planck's constant $\hbar$, and the electron mass m_e all set to unity. The i and j summations range over the n_b discrete bands (orbitals) included in the triply periodic calculation for the cubic supercell volume element Ω. The α sum is over the three spatial directions and improves the statistics. $F(\epsilon_{i,\mathbf{k}})$ is the Fermi weight corresponding to the energy $\epsilon_{i,\mathbf{k}}$ for the ith band at **k**. In practice, because of the finite simulation volume and resulting discrete eigenvalues, the δ-function must be broadened. We use a Gaussian broadening of the δ-function that is as small as feasible without recovering the local oscillations in the optical conductivity resulting from the discrete band structure [26]. A good initial starting point for the width of the Gaussian is the average of the nearest neighbor change in the eigenvalues, weighted by the corresponding change in the Fermi function [26]. The application of the Kubo-Greenwood formulation was exclusively conducted using the PAW potentials as it avoids the computation of the nonlocal components that plagues the use of pseudopotential approaches in the calculation of the optical properties. For the calculation of the optical properties using the PAW formulation, the plane-wave cutoff energy was 180 eV.

An important and useful check on the consistency of the optical conductivity calculation is the well-known sum rule [42]

$$S \equiv \frac{2\Omega}{\pi N_e}\int_0^\infty \sigma(\omega)d\omega = 1. \tag{3}$$

Since the low frequency part of $\sigma(\omega)$ converges with increasing number of bands, n_b, much faster than the high frequency tail, the dc conductivity converges well before the sum rule. We maintained a sufficient number of bands to satisfy the sum rule to at least within 7%, and typically much better (2%), which means that the dc conductivities are converged to an even higher degree.

Further details and results of the Kubo-Greenwood calculations of the real part of the optical conductivity can be found in Ref. [26]. We consider now the complete set of optical properties that can be determined from the optical conductivity. While the Rosseland mean opacities still find ample use in many macroscopic models and provide systematic means for comparisons among various formulations, the advent of more elaborate radiation-hydrodynamics packages dictates a new emphasis on the frequency dependence of the absorption process. As such, we will employ the absorption coefficient (also called frequency dependent opacity), the index of refraction in addition to the Rosseland mean opacity to describe the optical properties of the media.

The absorption coefficient and index of refraction follow directly from the knowledge of the real part of the optical conductivity and are defined as

$$\alpha(\omega) = \frac{4\pi}{n(\omega)c}\sigma_1(\omega),$$

$$n(\omega) = \sqrt{\tfrac{1}{2}[|\epsilon(\omega)| + \epsilon_1(\omega)]}. \quad (4)$$

The dielectric functions are, in turn, immediately obtained from the two parts of the conductivity,

$$\epsilon_1(\omega) = 1 - \frac{4\pi}{\omega}\sigma_2(\omega), \quad (5)$$

$$\epsilon_2(\omega) = \frac{4\pi}{\omega}\sigma_1(\omega), \quad (6)$$

while the imaginary part, $\sigma_2(\omega)$ arises from the application of a Kramers-Kronig relation as

$$\sigma_2(\omega) = -\frac{2}{\pi}\mathrm{P}\int \frac{\sigma_1(\nu)\omega}{(\nu^2-\omega^2)}d\nu. \quad (7)$$

In Eq. (7) P stands for the principal value of the integral.

Finally, the Rosseland mean opacity is given as [49]

$$1/\kappa_R(\rho,T) = \frac{\int_0^\infty d\nu n^2(\nu)[\partial B(\nu,T)/\partial T]/\alpha(\rho,T,\nu)}{\int_0^\infty d\nu n^2(\nu)B(\nu,T)}. \quad (8)$$

where the derivative of the normalized Planck function is written as

$$\partial B(\nu,T)/\partial T = [15/(4\pi^4 T)][u^4 e^u/(e^u-1)^2]. \quad (9)$$

The dimensionless variable u equals $h\nu/T$, with $h\nu$ the photon energy and T the temperature of the media in energy units. $\partial B(\nu,T)/\partial T$ is a slowly varying function that peaks around $4k_BT$.

III. RESULTS

A. Equation of state (EOS)

The accurate calculation of the optical properties of a plasma relies on a precise description of the corresponding material properties such as the equation of state (EOS). The QMD approach, while extremely expensive computationally, includes without approximation, transient effects such as dissociation or association of chemical bonds, and ionization or recombination. Consequently, the total pressure reflects not only the constituency of the fluid at a given temperature and density but also various density effects. In contrast, density effects such as pressure ionization, which describes the influence of the surrounding environment on the population of the isolated atomic states, only enter in atomic modeling code in phenomenological fashion.

We show in Fig. 1, the QMD 10 000 K and 30 000 K isotherms over two orders of magnitude in densities. First,

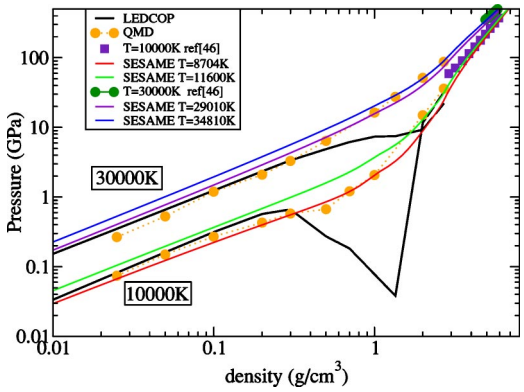

FIG. 1. (Color online) Comparison of the QMD aluminum isotherms with various standard EOS models.

for the whole density range and for both isotherms, we find a remarkable agreement between the QMD and the predictions of the best current SESAME EOS for aluminum [44,45], and another aluminum EOS developed for high densities using a combination of lattice dynamics, Wallace's liquid dynamics, and density functional theory [46]. This comparison clearly shows that QMD captures the physical processes in action as the media evolves throughout this density span. For densities below 0.1 g/cm^3, we also find good agreement between the QMD isotherm and the result of the Los Alamos Detailed Configuration Opacity Program (LEDCOP) [47,48]. LEDCOP employs an EOS model based on the Saha equation with detailed energy levels associated with each ion stage. Minimization of the associated free energy produces ion abundances, bound state occupations, and number of free electrons while density effects, arising from the influence of the surrounding media, appear through perturbative adjustments [3,49].

As the density increases and density effects become more important, the LEDCOP isotherms drastically deviate from the other calculations. For densities between 0.2 g/cm^3 and 2.0 g/cm^3 the inaccuracies in LEDCOP can be traced back to limitations in the EOS model. In this regime, the effect of the environment on the atomic system can no longer be treated as a perturbation. It should also be pointed out that the LEDCOP EOS model, while appropriate for low density calculations, is here pushed outside of its range of validity. To further quantify the variation of the nature of the media as both the density and temperature are varied, we now consider the variation of the conductivity over the same physical conditions.

B. Electrical properties

The variation of the electrical conductivity of aluminum over this density region was extensively investigated using QMD simulations in Ref. [26]. (See also Refs. [29,13].) We recall here the main findings as they relate to the analysis of the EOS shown above and to the optical properties that will be presented in the following section. Using the Kubo-Greenwood formulation, the dc conductivity, σ_{dc}, is given as

$$\sigma_{\mathrm{dc}} = \lim_{\omega\to 0}\sigma_1(\omega). \quad (10)$$

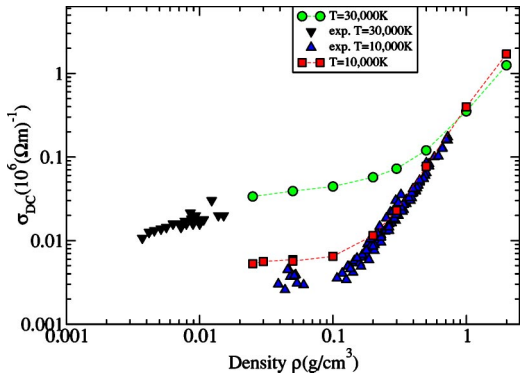

FIG. 2. (Color online) Variation of the QMD aluminum dc conductivity as a function of density for two isotherms: 10 000 K and 30 000 K. Calculation results from Ref. [26] are shown in red (squares) and green (circles), respectively; the corresponding data at 10 000 K and 30 000 K from exploding wire experiments [14] are shown in blue (inverted triangle) and black (triangle).

We show in Fig. 2, a comparison between the experimental data from exploding wires [14] and QMD conductivities from Ref. [26] along the same isotherms as in Fig. 1. As was pointed out in previous publications [13,26,29], at the highest density, 2 g/cm^3, the dc conductivity corresponds to that of a simple metal and decreases as expected as the temperature increases. At this density, the ac or optical conductivity calculated by QMD follows a Drude form and can be fitted with the following functional form [41]:

$$\sigma_1(\omega) \sim \frac{\sigma_{\rm dc}}{1+\omega^2\tau^2}, \tag{11}$$

where τ is the collisional relaxation time. Fitting $\sigma_1(\omega)$ with the functional form given above yields the value of $\sigma_{\rm dc}$ shown in Fig. 2 and τ [29]. In turn, this allows us to estimate the electron density,

$$n_e = \frac{m_e \sigma_{\rm dc}}{e^2 \tau}, \tag{12}$$

and the effective ionization fraction (charge carrier) $\bar{Z}$:

$$\bar{Z} = \frac{n_e \Omega}{N}, \tag{13}$$

with e and m_e, the charge and mass of an electron, respectively. At a density of 2 g/cm^3, this procedure leads to an ionization fraction, $\bar{Z}$, of about three, corresponding to the number of active electrons used in the calculation, and indicative of the metallic behavior of the system. At this density, the collisional relaxation time, τ, is found to be equal to 4.51×10^{-16} s and 3.32×10^{-16} s for a temperature of, respectively, 10 000 and 30 000 K. This average ionization fraction indicates that at this density, the plasma is strongly coupled ($\Gamma=10-50$) and of low degeneracy ($\theta=0.1$) [13]. Finally, these findings are supported by the calculated density of states (DOS) which does not show either a gap or minimum near the Fermi level [13,29].

It was noted in Ref. [26] that as the density is lowered further, the conductivity decreases as $\rho^{7/3}$ along each isotherm until it stabilizes at a mostly fixed value down to the lowest density explored. This behavior is seen in Fig. 2 as the high density envelope of the two isotherms. As was discussed in the earlier paper, the transition in the conductivity behavior corresponds to the appearance of a gap in the DOS at the Fermi energy, with the remaining conductivity resulting from the tail of the Fermi distribution across this gap. At 30 000 K and $\rho=0.025$ g/cm^3, an analysis of the optical conductivity, which follows a Drude form for photon energy less than 2 eV, gives an ionization fraction of 0.88 [26] and a collisional relaxation time, τ, of 24.3×10^{-16} s. This indicates that as the density is varied from 2.0 g/cm^3 to 0.025 g/cm^3, the ionization fraction of the system varies from a value of 3 to less than 1 along each isotherm while the collisional relaxation time, τ, increases by an order of magnitude. At 10 000 K, the ionization fraction was estimated to be $\bar{Z}\sim0.1$ ($\tau=33.64\times10^{-16}$ s).

This latter point is at the heart of the difficulty in calculating optical properties along the transition into the warm dense matter regime using standard opacities codes. From the above analysis, we can now interpret the failure of the LEDCOP EOS model shown in Fig. 1. At the lowest density point, the system is either mostly atomic for the lowest temperature, or singly ionized at the highest. As the environment only plays a perturbative role, the LEDCOP EOS is shown to be in good agreement with the other models. As the density increases along each isotherm, the pressure ionization model, which drives the delicate balance between the ionization and recombination processes now strongly perturbed by the environment, breaks down. In a typical opacity calculation, where the EOS is obtained by minimization of the free energy, the effect of increasing density results in further truncation of the highest atomic states in the partition function. In the present situation, atomic states need to be truncated smoothly to recover the metallicity and ionization fraction of the system at the highest density. This implies that all the excited states of the first three ionization stages of Al need to be removed at a density of 2 g/cm^3. Furthermore, the correlated nature of the state reached, especially at the lowest temperature, add an additional layer of difficulty in obtaining a correct expression for the free energy. With this understanding on the varied nature of the system in this density range, we now turn to the calculation of the corresponding optical properties using QMD.

C. Optical properties

We first investigate various trends in the absorption coefficient and index of refraction. At the lowest density $\rho=0.025$ g/cm^3 ($\sim10^{20}$ atoms/cm^3), the nature of the medium discussed above becomes clearer by examining in Fig. 3 the frequency-dependent absorption coefficient. We first note a prominent feature between 5 and 6 eV, depending on temperature. This feature was identified in Ref. [26] as the $3s\rightarrow3p$ transition in aluminum. At the lowest temperature, the position of this line at 5.1 eV is in good agreement with the average configuration energy for the $3s-3p$ transition in

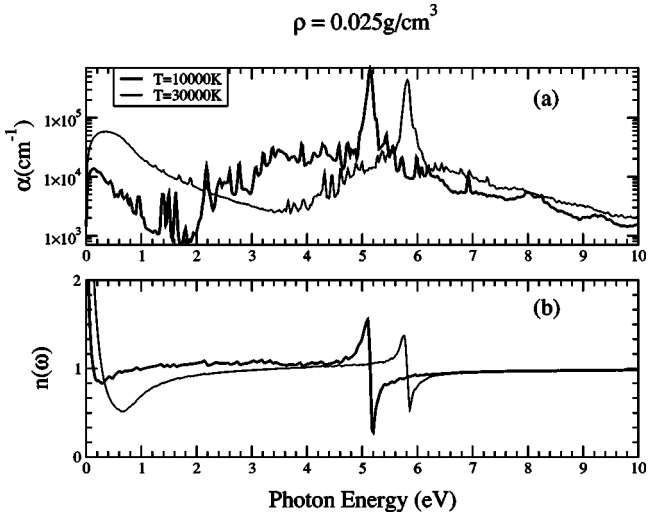

FIG. 3. (a) Absorption coefficient as a function of photon energy for a density of 0.025 g/cm^3 at temperatures of 10 000 K (dark solid line) and 30 000 K (light solid line). (b) Corresponding index of refraction.

neutral aluminum, 5.18 eV [50], consistent with the low ionization fraction discussed above. This identification of the maximum in the absorption coefficient is also supported by the variation of the index of refraction which shows a resonant profile at this particular energy. We recall from elementary atomic physics that for noninteracting atoms or ions [51], the dielectric function and, consequently, the resulting index of refraction exhibits a resonance profile of the form $1/(\omega_i^2-\omega^2)$ at the position of an isolated atomic line transition at ω_i. As the temperature rises to 30 000 K, Fig. 3 shows that the maximum shifts to an energy of ~5.8 eV and now corresponds to the $3s \rightarrow 3p$ transition in Al^+, in accordance with the analysis given above which indicates that the ionization fraction of the medium has increased to $(\bar{Z} \sim 1)$ [26].

For photon energies of a few eV, Fig. 3 also shows that the absorption coefficient rapidly increases. To interpret this feature, it is useful to recall that in a standard opacity calculation, this photon energy region is dominated by the free-free contribution (also called inverse Bremstrahlung). This effect stems from the photon scattering off free electrons subjected to the Coulomb field of an ion. At low density, a classical approximation of this effect, also known as the Kramers formula, indicates that the absorption coefficient behaves as

$$\sigma_1(\omega) \sim 1/\omega^3. \tag{14}$$

While the Kubo-Greenwood calculations do not explicitly separate each contribution to the total absorption coefficient, as is the case for a standard opacity calculation, a few observations clearly suggest that this effect is at play in this photon energy range. This interpretation is substantiated by first noting in Fig. 3 that the magnitude of this contribution increases proportionally to the ionization fraction. Figure 3(a) indicates that in this photon energy region, the absorption coefficients have a similar behavior and vary by an order of magnitude as the ionization fraction varies from 0.1 to 1. Second, an analysis of the QMD calculation indicates that the optical conductivity and, consequently the absorption coefficient, mostly results from the contribution of high lying excited states. Furthermore, while it is clear from Fig. 3 that the power law suggested by Eq. (14) is not followed by the QMD calculations, it is important to recall that Eq. (14) assumes a classical description of the electron-ion interaction, supposes an isolated system of three particles, namely a photon, an electron, and a charged ion, and no screening of the ion due to the influence of the surrounding media. In contrast, the formulation used in the present application, Eq. (2), represents the one-electron approximation to the optical conductivity as obtained within the rather general linear response theory [41,43]. In effect, this formulation supercedes the usual Kramers formula for the free-free contribution and latest quantum mechanical calculations of the free-free contribution start from the Kubo-Greenwood formulation where scattering cross sections for an isolated system are included to describe this effect [49,52,53].

As another example of the completeness of the approach proposed here in accounting for various effects influencing optical property calculations, we note in Fig. 3 that the absorption coefficient drastically decreases near the origin. This decrease in the absorption coefficient coincides with a value of the index of refraction less than 1 followed by a rapid increase as the photon energy approaches the origin. Recalling that for a simple metal, the optical conductivity obtained using a Drude model, Eq. (11), leads, using Eqs. (5) and (6), to a dielectric function of the form

$$\epsilon^{\mathrm{Drude}}(\omega) = 1 - \frac{\omega_p^2}{\omega^2 + 1/\tau^2} + i\frac{\omega_p^2}{\omega\tau(\omega^2 + 1/\tau^2)}, \tag{15}$$

where ω_p, the plasma frequency is given by

$$\omega_p^2 = \frac{4\pi n_e e^2}{m_e}. \tag{16}$$

This functional form of the dielectric function first shows that the real part of $\epsilon(\omega)^{\mathrm{Drude}}$ goes through zero in the vicinity of the plasma frequency. Using (4), this functional form leads to the behavior of the index of refraction shown in Fig. 3(b) for photon energy less than 2 eV, with a minimum at frequencies close to the plasma frequency of the system. For an ionization fraction $\bar{Z}$ of 0.1 (T=10 000 K) and 1 (T=30 000 K), relation (16) estimates the plasma frequency at $\omega_p^{10\,000\ \mathrm{K}}$=0.27 eV and $\omega_p^{30\,000\ \mathrm{K}}$=0.87 eV in good agreement with the behavior of the index of refraction shown in Fig. 3(b). As for a simple metal, the rapid increase of the index of refraction below the plasma frequency indicates that propagation is no longer sustained by the media below this frequency.

In summary, the analysis of the QMD absorption coefficient at this low density shows that the atomic and plasma effects needed for the calculation of the optical properties are naturally embodied within the method. As pointed out before [54], we also note that the current formulation does not allow for spectroscopic accuracy and only provides an average of all the transitions belonging to a given atomic configuration. This aspect renders the method of little use at very low den-

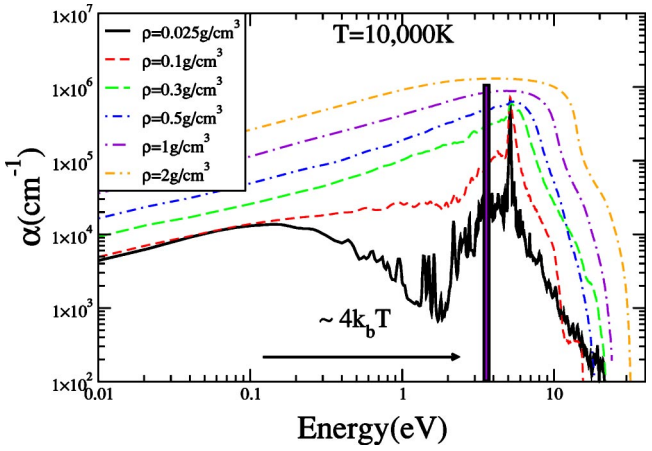

FIG. 4. (Color online) Absorption coefficients $\alpha(\omega)$ as a function of photon energy at $T=10\,000$ K for a span of densities (g/cm^3): 0.025 (solid line); 0.1 (dashed line); 0.3 (dotted line); 0.5 (dashed-dashed-dotted line); 1.0 (dashed-dotted line); and 2.0 (dotted-dotted-dashed line). Bar at $4k_BT$ represents maximum region of contribution to the Rosseland mean κ_R.

sities where spectroscopic resolution is a prerequisite. At the densities of interest in the present work, the method does however gives an adequate description of the optical properties provided that, as it is the case for aluminum here, the energy of the transition given by the FT-DFT formulation is in agreement with the transition average for the corresponding configuration. We now turn to the behavior of the absorption coefficient and index of refraction as the density gradually increases up to solid density.

Figures 4 and 5 show the variation of the absorption coefficient and index of refraction along the 10 000 K isotherm. We see in Fig. 4, that the atomic transition line at 5.1 eV identified above at a density of $\rho=0.025$ g/cm^3, gradually broadens and vanishes as the density increases to 0.3 g/cm^3. This corresponds to the gradual increase in the ionization fraction of the media, illustrated in Fig. 2 by the rise in conductivity. As the density increases to 0.3 g/cm^3,

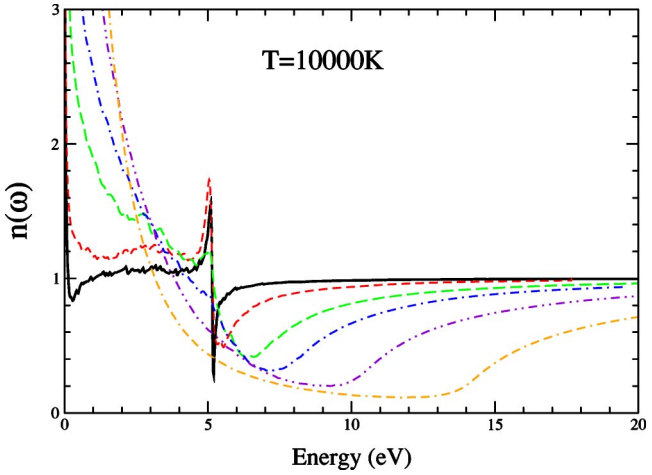

FIG. 5. (Color online) Index of refraction $n(\omega)$ as a function of frequency at $T=10\,000$ K for a span of densities. Same legend as in Fig. 4.

the gradual filling of the valley around 2 eV in Fig. 4 corresponds to the closure of the band gap pointed out above at this density region. As the density is further increased up to solid density, $\rho=2$ g/cm^3, the absorption coefficient resembles the optical response of a simple metal as given by the Drude theory. This gradual transition of the optical properties of a mostly atomic system to the one of a typical metal of ionization fraction, $\bar{Z}\sim 3$, is even better illustrated by inspection of the corresponding index of refraction shown in Fig. 5.

At a density of 0.3 g/cm^3, the index of refraction still shows a mild maximum at a photon energy of about 5 eV but with now a marked minimum at about 6–7 eV which corresponds as before to the plasma frequency at this density. As the density is further increased, the maximum of the index of refraction, corresponding to the position of the $3s\rightarrow 3p$ atomic transition, rapidly disappears while the minimum, which now becomes the prominent feature, progresses to higher photon energy. At the highest density, $\rho=2$ g/cm^3, the plasma frequency given by Eq. (16) and corresponding to an ionization fraction $\bar{Z}=3$ is 13.52 eV, in fair agreement with the behavior of the index of refraction shown in Fig. 5. Figures 4 and 5 exemplify the usefulness of the method at describing the variation of the optical properties for conditions corresponding to the transition to the warm dense matter regime where the isolated atom optical properties are gradually replaced by the one of a simple metal.

We finally turn to a direct comparison of the Rosseland mean opacities obtained using QMD and the standard opacity code LEDCOP. In the LEDCOP opacity code, the energy-dependent absorption coefficients are obtained by combining the EOS shown in Fig. 1 with the appropriate isolated atom photoionization (bound-free), inverse Bremstrahlung (free-free), scattering cross sections, and bound-bound transition arrays [47,48]. Figure 6(a) shows the variation of the Rosseland mean opacity for a fixed temperature of $T=10\,000$ K and as the density varies from 0.025 g/cm^3 to 2 g/cm^3. At the lowest density, $\rho=0.025$ g/cm^3, we find very good agreement between the two calculations. This good agreement can be explained by noticing that at this temperature, the Rosseland mean opacity probes the absorption coefficient at photon energies around 3.5 eV. Figure 3 shows that the $3s\rightarrow 3p$ transition does not influence significantly the Rosseland mean opacity in this photon energy region. At this temperature-density point, we also note that the ionization fractions given by the two calculations are in good agreement and around $\bar{Z}=0.1$. As the density increases and the LEDCOP calculation approaches its limit of validity, $\rho=0.1$ g/cm^3, Fig. 6 shows that the two calculations of the Rosseland mean depart. This increasing difference can be traced back to the limitation of the pressure ionization model in LEDCOP and how the effect of continuum lowering is accounted for. In contrast, the QMD calculation indicates that the increase in charge carriers is much more gradual. Beyond a density of 0.1 g/cm^3, the QMD calculation shows a rapid rise in the Rosseland mean opacity. This rise coincides with the closure of the band gap and the associated metallization of the system. We also note that this increase in the Rosseland mean opacity appears at densities where Fig. 2

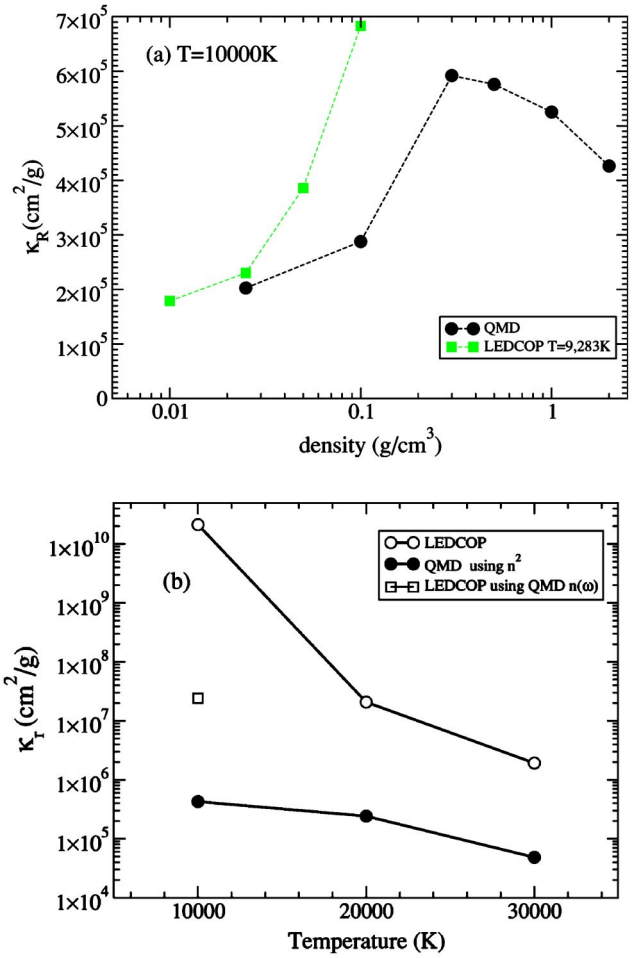

FIG. 6. (Color online) Variation of the LEDCOP and QMD Rosseland mean opacities (a) as a function of density and for a fixed temperature of $T=10\,000$ K, (b) as a function of temperature and for a fixed density of $\rho=2$ g/cm^3.

shows that the associated dc conductivity rapidly increases.

We show in Fig. 6(b) a comparison of the LEDCOP and QMD calculations at solid density, $\rho=2$ g/cm^3, and as a function of increasing temperature. Figure 6(b) shows that the biggest disagreement exists, as expected, at the lowest temperature. At 10 000 K, the LEDCOP Rosseland mean is dominated by the free-free contribution, described using the classical Kramer relation Eq. (14). In addition, the $1/\omega^3$ behavior near the origin is somewhat tempered by approximating the index of refraction as a step function rising to unity at the plasma frequency. In contrast, the QMD calculations shown in Figs. 4 and 5 indicate that the absorption coefficient and index of refraction behave as a simple metal. As previously noted for the case of hydrogen [20], we show in Fig. 6 that some improvements in the LEDCOP mean opacity can be obtained by using an index of refraction following a Drude functional form. At 10 000 K, we used the QMD index of refraction obtained at this condition. This procedure significantly improves the LEDCOP Rosseland mean opacity. As the temperature increases and the Rosseland mean opacity probes the absorption coefficient closer to the plasma frequency, the agreement between the LEDCOP and QMD calculations somewhat improves but still point to the failure of the Kramer relation for the free-free contribution in this regime.

IV. CONCLUSION

We have shown that QMD simulations provide an efficient mean to calculate the optical properties of aluminum for densities characteristic of the transition into the warm dense matter regime. The QMD method is computationally expensive and can only be applied to a limited density-temperature region compared to atomic modelling codes. We show, however, that it provides a powerful tool to validate plasma models used in atomic physics approaches in the warm dense matter regime by providing a consistent set of material, electrical and optical properties from the same simulation.

ACKNOWLEDGMENTS

Work supported under the auspices of the U.S. Department of Energy at Los Alamos National Laboratory under Contract No. W-7405-ENG-36. Sandia is a multiprogram laboratory operated by Sandia Corporation, a Lockheed Martin Company for the United States Department of Energy's National Nuclear Security Administration under Contract DE-AC04-94AL85000.

[1] G. W. Collins *et al.*, Science **281**, 1178 (1998) and references therein.
[2] J. D. Lindl, R. L. McCoy, and E. M. Campbell, Phys. Today **45**(9), 32 (1992).
[3] C. A. Iglesias *et al.*, Astrophys. J. Lett. **569**, L111 (2002).
[4] G. Fontaine *et al.*, Publ. Astron. Soc. Pac. **113**, 409 (2001).
[5] M. D. Knudson, D. L. Hanson, J. E. Bailey, C. A. Hall, and J. R. Asay, Phys. Rev. Lett. **87**, 225501 (2001); **90**, 035505 (2003); M. D. Knudson, D. L. Hanson, J. E. Bailey, C. A. Hall, J. R. Asay, and C. Deeney, Phys. Rev. B **69**, 144209 (2004).
[6] S. T. Weir, A. C. Mitchell, and W. J. Nellis, Phys. Rev. Lett. **76**, 1860 (1996); W. J. Nellis, S. T. Weir, and A. C. Mitchell, Phys. Rev. B **59**, 3434 (1999); R. Chau, A. C. Mitchell, R. W. Minich, and W. J. Nellis, Phys. Rev. Lett. **90**, 245501 (2003).
[7] P. M. Celliers, G. W. Collins, L. B. Da Silva, D. M. Gold, R. Cauble, R. J. Wallace, M. E. Foord, and B. A. Hammel, Phys. Rev. Lett. **84**, 5564 (2000); D. G. Hicks, P. M. Celliers, G. W. Collins, J. H. Eggert, and S. J. Moon, *ibid.* **91**, 035502 (2003).
[8] A. N. Mostovych and Yung Chan, Phys. Rev. Lett. **79**, 5094 (1997).
[9] B. J. Siwick, J. R. Dwyer, R. E. Jordan, and R. J. D. Miller, Science **302**, 1382 (2003).
[10] C. Guo, G. Rodriguez, A. Lobad, and A. J. Taylor, Phys. Rev. Lett. **84**, 4493 (2000).

[11] J. F. Benage, Phys. Rev. Lett. **83**, 2953 (1999).
[12] J. P. Chittenden *et al.*, Phys. Rev. E **61**, 4370 (2000).
[13] V. Recoules, P. Renaudin, J. Clerouin, P. Noiret, and G. Zerah, Phys. Rev. E **66**, 056412 (2002).
[14] A. W. De Silva and J. D. Katsouros, Phys. Rev. E **57**, 5945 (1998).
[15] J. P. Cox and Giulli, *Principles of Stellar Structure* (Gordon & Breach, London, 1968).
[16] T. Blensky, Astrophys. J., Suppl. Ser. **127**, 239 (2000).
[17] L. Collins, I. Kwon, J. Kress, N. Troullier, and D. Lynch, Phys. Rev. E **52**, 6202 (1995); L. Collins, J. Kress, T. Lenosky, N. Troullier, and I. Kwon, J. Comput.-Aided Mater. Des. **5**, 173 (1998).
[18] D. Hohl, V. Natoli, D. M. Ceperley, and R. M. Martin, Phys. Rev. Lett. **71**, 541 (1993); J. I. Penman, J. Clerouin, and G. Zerah, Phys. Rev. E **51**, R5224 (1994); J. Kohanoff and J-P. Hansen, *ibid.* **54**, 768 (1995); O. Pfaffenzeller and D. Hohl, J. Phys.: Condens. Matter **9**, 11023 (1997); G. Galli, R. Hood, A. Hazi, and F. Gygi, Phys. Rev. B **61**, 909 (2000); S. Bagnier, P. Blottiau, and J. Clerouin, Phys. Rev. E **63**, 015301 (2000).
[19] L. Collins, S. Bickham, J. Kress, S. Mazevet, T. Lenosky, and W. Windl, Phys. Rev. B **63**, 184110 (2001).
[20] S Mazevet, L. Collins, N. Magee, J. Kress, and J. Keady, Astron. Astrophys. **405**, L5 (2003).
[21] T. Lenosky, S. Bickham, J. Kress, and L. Collins, Phys. Rev. B **61**, 1 (2000).
[22] M. P. Desjarlais, Phys. Rev. B **68**, 064204 (2003).
[23] J. Kress, S. Mazevet, L. Collins, and W. Wood, Phys. Rev. B **63**, 024203 (2001).
[24] S. Mazevet, J. D. Johnson, J. D. Kress, L. A. Collins, and P. Blottiau, Phys. Rev. B **65**, 014204 (2002).
[25] S. Mazevet, J. Kress, P. Blottiau, and L. Collins, Phys. Rev. B **67**, 054201 (2003).
[26] M. P. Desjarlais, J. D. Kress, and L. A. Collins, Phys. Rev. E **66**, 025401 (2002).
[27] S. Mazevet, P. Blottiau, J. D. Kress, and L. A. Collins, Phys. Rev. B **69**, 224207 (2004).
[28] Y. Laudernet, J. Clerouin, and S. Mazevet, Phys. Rev. B **70**, 165108 (2004).
[29] P. L. Silvestrelli, Phys. Rev. B **60**, 16382 (1999).
[30] D. K. Kim and I. Kim, Phys. Rev. E **68**, 056410 (2003).
[31] C. Blancard and G. Faussurier, Phys. Rev. E **69**, 016409 (2004).
[32] G. Kresse and J. Hafner, Phys. Rev. B **47**, RC558 (1993); G. Kresse and J. Furthmüller, Comput. Mater. Sci. **6**, 15 (1996); Phys. Rev. B **54**, 11169 (1996).
[33] N. D. Mermin, Phys. Rev. **137**, A1441 (1965).
[34] J. P. Perdew, in *Electronic Structure of Solids*, edited by F. Ziesche and H. Eschrig (Akademie Verlag, Berlin, 1991).
[35] D. Vanderbilt, Phys. Rev. B **41**, 7892 (1990).
[36] G. Kresse and J. Hafner, J. Phys.: Condens. Matter **6**, 8245 (1994).
[37] G. Kresse and J. Joubert, Phys. Rev. B **59**, 1758 (1999).
[38] P. E. Blöchl, Phys. Rev. B **50**, 17953 (1994).
[39] H. J. Monkhorst and J. D. Pack, Phys. Rev. B **13**, 5188 (1976).
[40] A. Baldereschi, Phys. Rev. B **7**, 5215 (1973).
[41] W. A. Harrison, *Solid State Theory* (Mc Graw-Hill, New York, 1970).
[42] G. D. Mahan, *Many Particle Physics* (Plenum, New York, 1981).
[43] J. Callaway, *Quantum Theory of the Solid State* (Academic, New York, 1974).
[44] SESAME EOS 3720, found in S. P. Lyon and J. D. Johnson, "T-1 Handbook of the SESAME Equation of State Library," LANL Report No. LA-CP-98-100.
[45] S. Crockett (private communication).
[46] E. Chisolm, S. Crockett, and D. Wallace, Phys. Rev. B **68**, 104103 (2003).
[47] N. Magee *et al.*, Astron. Soc. Pac. Conf. Ser. **78**, 51 (1995).
[48] C. Neuforge-Verheecke, J. Guzik, J. Keady, N. Magee, P. Bradley, and A. Noels, Astrophys. J. **561**, 450 (2001).
[49] F. Perrot, Laser Part. Beams **14**, 731 (1996).
[50] W. C. Martin and R. Zalubas, J. Phys. Chem. Ref. Data **8**, 817 (1979).
[51] J. D. Jackson, *Classical Electrodynamics*, 2nd ed. (Wiley, New York, 1965).
[52] C. Iglesias and F. Rogers, Astrophys. J. **464**, 943 (1996).
[53] B. Crowley and J. Harris, J. Quant. Spectrosc. Radiat. Transf. **71**, 257 (2001).
[54] R. Singh and B. M. Deb, Phys. Rep. **311**, 47 (1999) and references therein.